Astronomy & Astrophysics

Photon-dominated region modeling of the CO and [C I] line emission in Barnard 68

J. L. Pineda[*] and F. Bensch

Argelander Institut für Astronomie, Universität Bonn, Auf dem Hügel 71, 53121 Bonn, Germany
e-mail: jopineda@astro.uni-bonn.de

ABSTRACT

Aims. We use the Barnard 68 dark globule as a test case for a spherically symmetric PDR model exposed to low-UV radiation fields. With a roughly spherical morphology and an accurately determined density profile, Barnard 68 is ideal for this purpose. The processes governing the energy balance in the cloud surface are studied in detail.

Methods. We compare the spherically symmetric PDR model by Störzer, Stutzki & Sternberg (1996) to observations of the three lowest rotational transitions of ^{12}CO, ^{13}CO $J = 2 \rightarrow 1$, and $J = 3 \rightarrow 2$, as well as the [C I] ^{3}P$_1 \rightarrow ^3$P$_0$ fine structure transition. We study the role of polycyclic aromatic hydrocarbons (PAHs) in the chemical network of the PDR model and consider the impact of depletion, as well as of a variation in the external FUV field.

Results. We find it difficult to simultaneously model the observed ^{12}CO and ^{13}CO emission. The ^{12}CO and [C I] emission can be explained by a PDR model with an external FUV field of 1-0.75χ_0, but this model fails to reproduce the observed ^{13}CO by a factor of ~2. Adding PAHs to the chemical network increases the [C I] emission by 50% in our model but makes [C II] very faint. The CO depletion only slightly reduces the ^{12}CO and ^{13}CO line intensity (by $\lesssim$10% and $\lesssim$20%, respectively). Predictions for the [C I] ^{2}P$_{3/2} \rightarrow ^2$P$_{1/2}$, [C I] ^{3}P$_2 \rightarrow ^3$P$_1$, and ^{12}CO $J = 5 \rightarrow 4$ and 4$\rightarrow$3 transitions are presented. This allows a test of our model with future observations (APEX, NANTEN2, HERSCHEL, SOFIA).

Key words. astrochemistry – ISM: molecules – ISM: individual objects: Barnard 68 – ISM: clouds

1. Introduction

The interest in photon-dominated regions (PDRs) is that they account for much of the line and continuum radiation from the molecular interstellar medium (ISM) of nearby star-forming regions to clouds in the diffuse Galactic radiation field at millimitre, sub-millimitre, and far-infrared wavelengths. Many numerical codes have been developed to model their emission and to understand the physical and chemical processes governing them (Hollenbach & Tielens 1999). Typically, PDR models use a physical structure (morphology, density profile) to calculate a self-consistent solution for the chemistry (abundance of species) and the energy balance (heating and cooling). Practically speaking, the numerical codes differ in the scope of the chemical networks and their reaction rates, as well as in the degree of sophistication with which the heating, cooling, and the radiative transfer are calculated. In many cases the goal of the PDR modeling is to constrain the physical properties of the line-emitting region (for example, its density and column density) and the strength of the external far-ultraviolet (FUV) field. PDR models successfully account for much of the line and continuum emission from Galactic and extra-galactic PDRs at millimitre, sub-millimitre, and far-infrared wavelengths (Hollenbach & Tielens 1997, 1999).

The coupling of the energy balance (heating & cooling) and the chemistry keeps PDR modeling from being a straight-forward task, however. In particular, a large set of non-linear equations needs to be solved in order to obtain abundance profiles of species. Small changes in the initial elemental abundances or the reaction rates of individual reactions within their sometimes large error margins can result in large variations in the abundance profiles of individual species (Röllig et al. 2007). In some regions of the parameter space, more than one steady-state solution to the chemical network may exist (bistability, e.g. Le Bourlot et al. 1993). Additional complications arise from intrinsic variations in published PDR models, which are noted even when identical source parameters and chemical reaction rates are used. The benchmarking study (Röllig et al. 2007) has shown that, even for constant density, plane-parallel models, the emerging line intensity of different numerical codes vary by up to an order of magnitude for some of the fine-structure transitions. These discrepancies very likely reflect both the different numerical methods used to solve the chemical structure and the numerical implementation of physical processes. The calibration of PDR models cannot be done easily since the observed clouds generally have more complex morphologies than assumed in most PDR models. It is therefore desirable to study clouds with a well-known geometry (density profile), which can be used to calibrate PDR models. For example, numerous PDR models have been made for the Orion Bar because of its approximate plane-parallel geometry (e.g. Tielens & Hollenbach 1985; Hollenbach & Tielens 1999).

Barnard 68 is an example where the density profile is constrained to a very high precision (Alves et al. 2001), and its geometry is well-matched to a spherically-symmetric PDR model. With no young stars nearby, the external FUV field is low, close to the level of the diffuse Galactic radiation field. Due to its

---

Table 1. Spectral line observations toward Barnard 68.

Telescope	Transition	Frequency GHz	# of positions	Sampling [arcsec]	θ_{mb}	η_{mb}	Δv [km s^{-1}]
SWAS	[C I] $^3P_1 \rightarrow ^3P_0$	492.160	1	–	258	0.9	0.623
Mopra	^{12}CO $J = 1 \rightarrow 0$	115.271	144	15	33	0.42	0.08
KOSMA	^{12}CO $J = 2 \rightarrow 1$	230.538	49	60	130	0.76	0.1
KOSMA	^{12}CO $J = 3 \rightarrow 2$	345.795	49	60	80	0.78	0.294
KOSMA	^{12}CO $J = 3 \rightarrow 2$	345.795	1	–	80	0.78	0.024
CSO[1]	^{13}CO $J = 2 \rightarrow 1$	220.398	65	24	33	0.70	0.06
CSO[1]	^{13}CO $J = 3 \rightarrow 2$	330.587	144	24	22	0.75	0.04

[1] Published by Bergin et al. (2006).

proximity to the Ophiuchus complex, we adopt a distance to the cloud of 125 pc (de Geus et al. 1989). Using near-infrared extinction techniques, Alves et al. (2001) derived an extinction map that was used to constrain the radial density profile of the cloud, suggesting that Barnard 68 is consistent with a pressure-confined self-gravitating cloud near equilibrium, a Bonnor-Ebert sphere. By avoiding the uncertainly concerning the geometry and density structure, we are able to study in detail the impact of the chemistry in the predicted line emission of the model.

Here, we present observations of the three lowest rotational transitions of ^{12}CO, the [C I] $^3P_1 \rightarrow ^3P_0$ fine-structure transition of neutral carbon, ^{13}CO $J = 2 \rightarrow 1$, and ^{13}CO $J = 3 \rightarrow 2$ and compare them to the KOSMA-τ spherical PDR model originally published by Störzer et al. (1996). The observations are summarized in Sect. 2. Section 3 describes the employed model, and the results are discussed in Sect. 4. In Sect. 5 the gas heating and cooling is studied and predictions of the intensity for other important cooling lines are made. A summary is given in Sect. 6.

2. Observations

Observations were made for the three lowest rotational transitions of CO and the [C I] $^3P_1 \rightarrow ^3P_0$ fine-structure transition of neutral carbon in Barnard 68. Additionally, we used the ^{13}CO $J = 3 \rightarrow 2$ and $J = 2 \rightarrow 1$ rotational transitions observed with the CSO telescope and published by Bergin et al. (2006). Using these transitions we deliberately limited ourselves to surface tracers, since the goal of this paper is to model of the PDR emission of a cloud in the diffuse Galactic radiation field.

The high signal-to-noise [C I] $^3P_1 \rightarrow ^3P_0$ observation was made in 2001 with the Submillimiter Wave Astronomy Satellite (SWAS[1]) with an angular resolution of 4'.3. It was pointed at a position ($\Delta\alpha = -0'.094$, $\Delta\delta = +0'.2$) offset from the column density peak of Barnard 68 at $\alpha = 17^h22^m38^s.6$ and $\delta = -23°49'46''.0$ (J2000) (Di Francesco et al. 2002) and essentially covers the whole cloud. The rms noise ΔT_{mb} is 23 mK per velocity channel ($\Delta v = 0.623$ km s^{-1}). A 3rd-order polynomial was fitted and subtracted from the spectra. SWAS simultaneously observed the transitions of four species, [C I] $^3P_1 \rightarrow ^3P_0$ at 492 GHz, ^{13}CO $J = 5 \rightarrow 4$ at 550.9 GHz, H_2O at 556.0 GHz, and O_2 at 487.2 GHz. No emission was detected for the last three species, however, and Bergin & Snell (2002) gave the resulting upper limits on the H_2O and O_2 column densities. The rms noise of the ^{13}CO $J = 5 \rightarrow 4$ spectrum was 13 mK per velocity channel.

The ^{12}CO $J = 1 \rightarrow 0$ (115 GHz) rotational transition was observed in June 2005 with the Mopra 22-m telescope located in Australia. A 6'×6' area was mapped using on-the-fly mode. The data were smoothed to an angular resolution of 1' on a grid with

a 30'' spacing. The resulting spectra typically have an rms noise ΔT_{mb} better than 0.5 K per velocity channel ($\Delta v = 0.08$ km s^{-1}). A straight line was fitted and subtracted from each spectrum.

The ^{12}CO $J = 2 \rightarrow 1$ (230 GHz) and ^{12}CO $J = 3 \rightarrow 2$ (345 GHz) transitions were mapped simultaneously with the 230/345 GHz dual-channel receiver at the KOSMA 3-m telescope toward 49 positions, spaced by 1'. For the ^{12}CO $J = 2 \rightarrow 1$ transition, 90% of the spectra have an rms noise ΔT_{mb} smaller than 0.3 K per velocity channel ($\Delta v = 0.1$ km s^{-1}). The ^{12}CO $J = 3 \rightarrow 2$ spectra are smoothed to the 130'' angular resolution of the 230 GHz beam, and 90% of the resulting spectra have an rms noise ΔT_{mb} smaller than 0.5 K per velocity channel ($\Delta v = 0.294$ km s^{-1}). Typically, a sinusoidal or 3rd-order polynomial was fitted and subtracted from each spectrum. Because of a small misalignment of both receiver channels, the pointing of the 345 GHz beam is offset by $\Delta AZ = -7''$ and $\Delta EL = +28''$ in horizontal coordinates relative to the lower frequency beam. The observations were completed within a relatively short period of time during the transit of the source. Thus, the offset in the horizontal system translates into an offset of approximately $\Delta\alpha = -7''$ and $\Delta\delta = -28''$ in equatorial coordinates, which was corrected in the final map. We estimate the accuracy of this correction to be within ~15''. The central position was also observed in the ^{12}CO $J = 3 \rightarrow 2$ line using the high-resolution spectrometer (HRS). The calibration of the KOSMA data was regularly checked and corrected using a source of known intensity (DR21). The observed spectra are shown in Fig. 2 and a summary of the observations is given in Table 1.

3. PDR model

We employ the spherically symmetric PDR model originally developed by Störzer et al. (1996) (KOSMA-τ model). This model uses a spherical cloud with a truncated power-law density profile and an isotropic FUV radiation field. We adopt a density profile of, $n(r) = n_s(r/r_c)^{-\alpha}$ for $0.3r_c \leq r \leq r_c$, and constant density, $n(r) = n_s(0.3)^{-\alpha}$ in the cloud center ($r < 0.3r_c$), for the present paper. Here, r_c is the cloud radius and n_s the density at the cloud surface. In our models we adopt a power-law exponent of $\alpha = 1.96$ for the density profile, a cloud surface density of 2×10^4 cm^{-3}, and a cloud radius of 1.9×10^{17} cm. This gives a reasonable fit to the measured column density profile for $r \lesssim 100''$, but does not account for the low-column density gas close to the surface at $100'' \lesssim r \lesssim 120''$ (Fig. 3). We tested the response of the emerging CO emission to small variations in the model cloud size. An extreme case is shown in Fig. 3 by the dotted line ($r_c = 2.09 \times 10^{17}$ cm), which matches the observed A_v at $100'' \lesssim r \lesssim 120''$, but overestimates the column density for $70'' \lesssim r \lesssim 100''$. The latter model produces CO emission that is typically stronger by only a few percent, however.

[1] See Melnick et al. (2000) for additional details about SWAS.
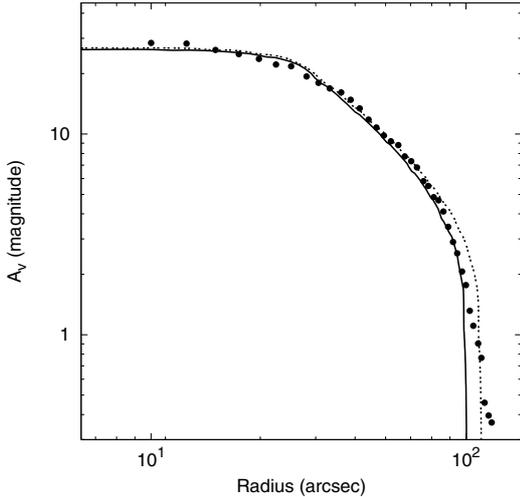
Fig. 1. Extinction profile for Barnard 68. Filled dots represent the measured A_v calculated by Alves et al. (2001), excluding the south east prominence seen in the visual extinction map. The solid line gives the line-of-sight extinction profile versus radius for the power-law density profile described in Sect. 4.1. The dashed line is the same column density profile for a model with the same density power-law index but a 10% larger radius.

Table 2. Standard model parameters.

Cloud surface density (cm^{-3})	2.01×10^4
Cloud radius (cm)	1.875×10^{17}
Exponent of the density power-law	1.96
Line Doppler width (km s^{-1})	0.11

The Doppler line-width in the model is $b = 0.11$ km s^{-1}, derived from the observed ^{13}CO $J = 2 \rightarrow 1$ line profile. The gas temperature measured using NH$_3$ observations toward Barnard 68 is 10–16 K (Hotzel et al. 2002a; Bourke et al. 1995). This suggests a pure thermal line width of 0.08–0.1 km s^{-1} for CO. The chemical network of the model includes H, He, C, O, N, plus a number of heavier elements, S, Si, Fe, and Mg. The ^{13}C is considered in the chemical network, including the isotope selective reactions for ^{13}CO. Self-shielding of ^{12}CO and ^{13}CO and shielding by H$_2$ against photo-destruction is implemented using the shielding factors by van Dishoeck & Black (1988). A summary of the model parameters is shown in Table 2 and the initial fractional abundances are listed in Table 3. Line intensities and line profiles are determined for the [C II] and the [C I] fine-structure transitions and for the ^{12}CO and ^{13}CO rotational transitions using the radiative transfer code by Gierens et al. (1992). For a comparison to the observed data, we smoothed the model intensity distribution and line profiles to the angular and velocity resolution of our observations. A summary of the models presented in this publication is shown in Table 4.

4. Result

4.1. Reference model

In the following, we define a reference model (Model #1a) with a strength of the external FUV field of $\chi = 1.0\chi_0$, where χ_0 is the intensity of the mean interstellar radiation field (Draine 1978). Our modeling goal is to match the observed line-integrated intensity and line profiles towards the cloud center and the azimuthally averaged intensity distribution. Table 5 shows the

Table 3. Fractional abundances[a].

He	0.1
C	1.32×10^{-4}
O	2.91×10^{-4}
N	8.5×10^{-5}
^{13}C	2.08×10^{-6}
S	1.87×10^{-6}
Mg	5.12×10^{-6}
Fe	6.19×10^{-6}
Si	8.21×10^{-7}
PAH[b]	1×10^{-7}

[a] Abundance relative to H nuclei.
[b] Not included in the reference model.

Table 4. Summary of PDR models.

Model #	FUV field χ_0	PAHs	Depletion
1a	1.0	N	N
1b	1.0	N	Y
2b	1.0	Y	Y
3a	0.75	Y	Y
3b	0.12	Y	Y

[C I], ^{12}CO, and ^{13}CO integrated intensity towards the cloud center (ratio of the model simulation to the observations).

Model #1a reproduces the line-integrated intensity toward the cloud center for the [C I] $^3P_1 \rightarrow {}^3P_0$, ^{12}CO $J = 1 \rightarrow 0$, and $J = 2 \rightarrow 1$ transition within 20%. However, the ^{12}CO $J = 2 \rightarrow 1$ and $J = 3 \rightarrow 2$ model line profiles show self-absorption, but this is not observed (Fig. 3).

We note that the ^{12}CO $J = 3 \rightarrow 2$ mapping observations for $r < 100''$ (Fig. 6) have a higher line intensity than the observation in Fig. 3 made toward the central position. The ^{12}CO observations made with a higher velocity resolution of ~0.1 km s^{-1} show a red line wing, with emission at velocities between 3.7 and 4.3 km s^{-1} (e.g. left panel of Fig. 3). This component cannot be modeled in the framework of a single, spherical clump; for a comparison to the PDR model simulations we therefore calculated the observed line-integrated intensity excluding this red line wing. This was not possible for the ^{12}CO $J = 3 \rightarrow 2$ mapping data because of the insufficient velocity resolution of the variable resolution spectrometer (VRS), and we expect that the line-integrated intensity of ^{12}CO $J = 3 \rightarrow 2$ in Fig. 6 is systematically overestimated. We estimate the magnitude of this effect to be on the order of 20%, based on our velocity-resolved ^{12}CO observations. Even with the line wing subtracted, however, the integrated intensity of the ^{12}CO $J = 3 \rightarrow 2$ HRS spectrum is about 40% lower than that for the corresponding VRS observations made at a different epoch. The integrated intensities of both observations only marginally agree within 3σ, given the error bars of ~16%. Despite a careful check of the pointing and calibration of the observations, we have to attribute a possible systematic error of up to ~40% to the $J = 3 \rightarrow 2$ data. This is likely to be due to the low elevation of the source during the observations (Barnard 68 transits at ≲20° elevation at the location of the KOSMA observatory). While the ^{12}CO $J = 3 \rightarrow 2$ VRS observations are consistent with the model, the HRS spectrum appears to be too weak by a factor of 0.5.

The largest discrepancy between the model and the observations is noted for the ^{13}CO emission, with line-integrated intensities in the model higher larger by 1.9 and 3.2 for the $J = 2 \rightarrow 1$ and $J = 3 \rightarrow 2$ transitions, respectively. Since the density profile
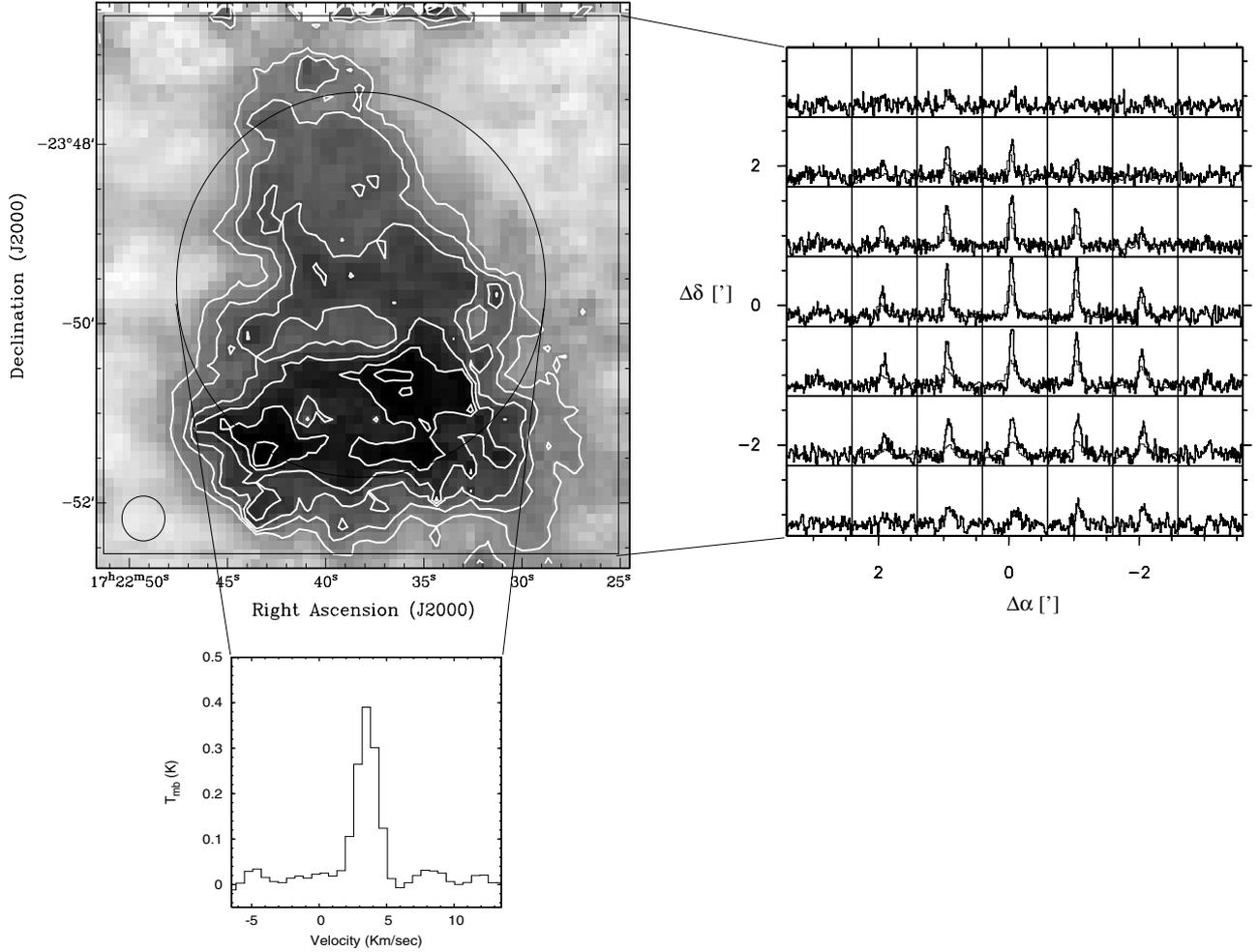
Fig. 2. *Upper left*: Map of the ^{12}CO $J = 1 \rightarrow 0$ emission of Barnard 68. The map is shown in its original resolution of $33''$. The contours run from 40% to 90% of the peak intensity (72.6 K km s^{-1}) in steps of 10%. *Upper right*: Spectra of the ^{12}CO $J = 2 \rightarrow 1$ (thick lines) and $J = 3 \rightarrow 2$ (thin lines) transitions with a resolution of $130''$. The velocity range is $v = 0 \ldots 8$ km s^{-1}, and the main-beam temperature shown is $T_{mb} = -1 \ldots 5$ K. The offset is given in arcminutes that are relative to the peak of the dust emission at $\alpha = 17^h22^m38\overset{s}{.}6$ and $\delta = -23°49'46\overset{''}{.}0$ (J2000). *Lower left*: [C I] $^3P_1 \rightarrow {}^3P_0$ emission toward the central position of Barnard 68. The $4\overset{'}{.}3$ beam size of SWAS covers a large fraction of the cloud.

Table 5. Model comparison with observations toward the Barnard 68 center.

Species transition	Telescope	Resolution ($''$)	I_{obs}^a	I_{model}/I_{obs}				
				Model #1a^b	Model #1b	Model #2b	Model #3a	Model #3b
[C I] $^3P_1 \rightarrow {}^3P_0$	SWAS	258	0.93 ± 5%	0.97	0.98	1.55	1.39	0.41
^{12}CO $J = 1 \rightarrow 0$	Mopra	60	0.11 ± 9%	1.08	0.99	0.87	0.82	0.51
^{12}CO $J = 2 \rightarrow 1$	KOSMA	130	0.47 ± 2%	1.24	1.18	1.10	1.00	0.54
^{12}CO $J = 3 \rightarrow 2$	KOSMA/HRS^b	80	0.72 ± 15%	2.26	2.14	2.03	1.56	0.68
^{12}CO $J = 3 \rightarrow 2$	KOSMA/VRS^b	80	1.41 ± 16%	1.15	1.09	1.03	0.80	0.35
^{13}CO $J = 2 \rightarrow 1$	CSO	33	0.19 ± 5%	1.92	1.56	1.38	1.30	0.94
^{13}CO $J = 3 \rightarrow 2$	CSO	22	0.25 ± 8%	3.19	2.57	2.13	1.95	1.27

^{a} The intensities are in units of 10^{-7} erg s^{-1} cm^{-2} sr^{-1}.
^{b} Observations made at different epochs with the high-resolution spectrometer (HRS) and the variable-resolution spectrometer (VRS).

of Barnard 68 is well-constrained, the discrepancies with the observations must have their origin in either the chemical network or the strength of the FUV radiation field.

4.2. Depletion

The observed line emission is significantly overestimated by the model for those transitions that probe somewhat deeper layers into the cloud surface, most notably the ^{13}CO transitions.

Observations of $C^{18}O$ and $C^{17}O$ in Barnard 68 reveal that CO, among other molecules, is depleted from the gas phase at $A_v \gtrsim 5$ due to freezing on dust grains (Hotzel et al. 2002b; Di Francesco et al. 2002; Bergin et al. 2006). In the present model, we studied the impact of the CO depletion on the line emission by truncating the ^{12}CO and ^{13}CO abundance profiles at $A_v = 5$ (setting the CO abundance to zero for $A_v \geq 5$; Model #1b). This is only a rough approximation, but it does allow us to assess the impact of depletion on the line emission. Figure 3 shows the ^{12}CO
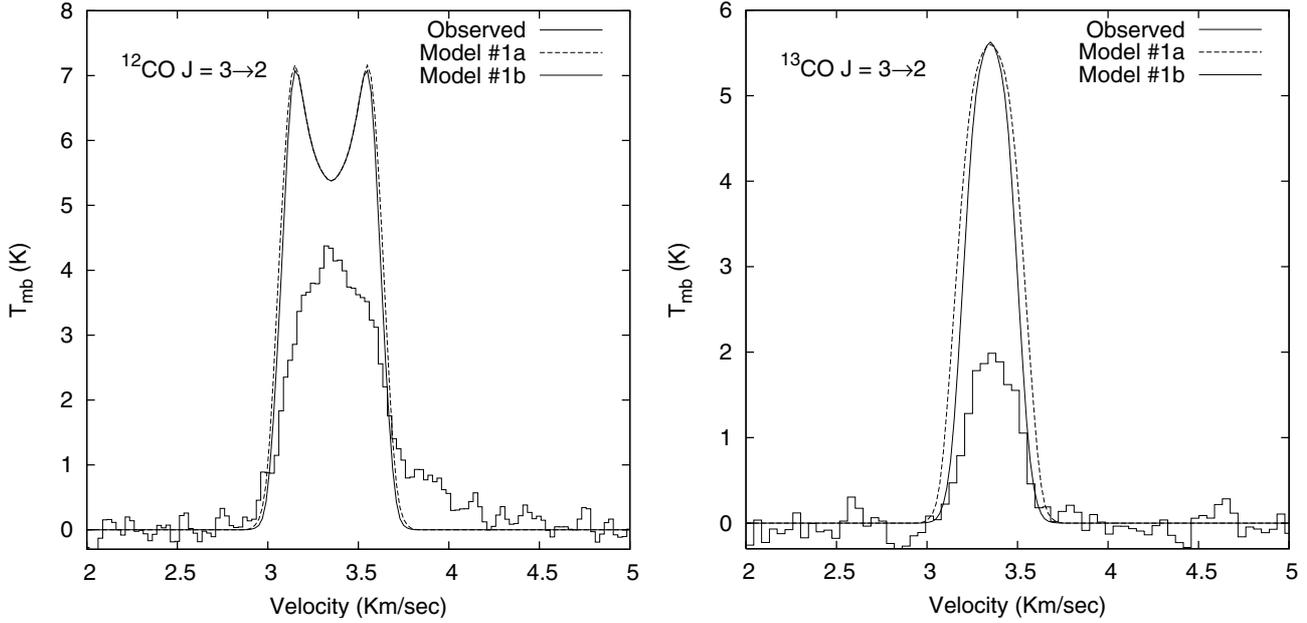
Fig. 3. Observed ^{12}CO and ^{13}CO $J = 3 \rightarrow 2$ line profiles. The reference model (Model #1a) and a model that considers the effects of depletion (Model #1b) are also shown.

and ^{13}CO $J = 3 \rightarrow 2$ line profiles for Models #1a and #1b; the resulting line-integrated intensities for the observed transitions are summarized in Table 5. The line-integrated intensities are lower by 10–20% in the model with depletion, mainly because the line profiles are narrower. We confirm that depletion plays a negligible role for low-J ^{12}CO emission and note a higher impact on both ^{13}CO transitions (20%) and the ^{12}CO $J = 3 \rightarrow 2$ transition (5%). However, the effect of depletion is much lower than the factor of 2 to 3 discrepancy noted between the observations and the model line intensities for ^{13}CO. Thus, depletion of CO cannot solely account for the low integrated intensity observed for the last transitions. In the following models (Model #2b, #3a, and #3b), we account for depletion in the same way as for Model #1b.

4.3. Polycyclic aromatic hydrocarbons

Polycyclic aromatic hydrocarbons (PAHs) are known to play an important role in the carbon chemistry, increasing the C column density and decreasing the CO abundance in the cloud surface (Lepp & Dalgarno 1988; Bakes & Tielens 1998). Following Kaufman et al. (1999), we included PAHs with an initial abundance of 1×10^{-7} relative to H nuclei and assuming an MRN (Mathis et al. 1977) size distribution for PAHs containing between 30 and 1500 carbon atoms. We considered neutral PAHs in our chemical network, their singly-charged variants (PAH$^+$, PAH$^-$), and PAHs with carbon and hydrogen ions adsorbed on their surface (PAHC$^+$, PAHH$^+$). We used a list of reactions provided by M. Kaufman (private communication) and calculated the reaction rates from the work of Draine & Sutin (1987) and Bakes & Tielens (1994). A comparison of the C$^+$, C^0, and CO abundance profiles and the gas temperature in the model with and without PAHs is shown in Fig. 4. We note that the results are relatively insensitive to the initial PAH abundance as long as PAHs are included. Models with a factor of 4 larger PAH abundance give similar line-integrated intensities (to within 10%). One of the main impacts of PAHs is that the C$^+$ layer at the cloud surface becomes thinner, increasing the

total atomic carbon column density. Close to the surface of the cloud, PAH$^-$ neutralizes with C$^+$, while CO is formed somewhat deeper into the cloud ($A_V > 0.4$). The higher neutral carbon column density (at $A_V < 0.5$; Fig. 4) and the higher gas temperature ($A_V < 0.2$) give a stronger [C I] emission compared to the model without PAHs. The CO line intensity is reduced in Model #2b because the emission traces a slightly colder region somewhat deeper into the cloud. The lower CO abundance at $A_V < 0.4$ in Model #2b also removes the self-absorption in the ^{12}CO $J = 2 \rightarrow 1$ line toward the cloud center and reduces it for the ^{12}CO $J = 3 \rightarrow 2$ line.

Model #2b gives [C I]/CO line ratios that are consistent with the observations and removes the ^{12}CO $J = 2 \rightarrow 1$ self-absorption noted in Model #1b. The ^{13}CO line intensities are significantly reduced in the model with PAH but are still a factor of 1.5–2.5 higher than the observations. The [C I] intensity is also overestimated by a factor of 1.5.

4.4. Variations in the radiation field

Generally, the line emission in the PDR model is reduced if a weaker external FUV radiation field is assumed. We explore the impact of lower external radiation field intensity as a next step. According to Bergin et al. (2006), the low ^{13}CO line intensities suggest that Barnard 68 is exposed to an FUV radiation field of rather low intensity, corresponding to $\chi = 0.12\chi_0$ (0.2 in units of the Habing (1968) field). We ran two additional models, the first with a somewhat lower $\chi = 0.75\chi_0$ (Model #3a) and a second with an intensity following Bergin et al. (2006) ($\chi = 0.12\chi_0$; Model #3b). All other model parameters are the same as for Model #2b. The observed CO line profiles and the model line profiles are shown in Fig. 5, and the radial profiles of the line-integrated intensity are given in Fig. 6. A comparison among the observed intensity profiles and the model is shown in Table 6. In order to quantify their difference, we calculated the average ratio of the model simulation to the observations for each observed position within $r < 100''$.
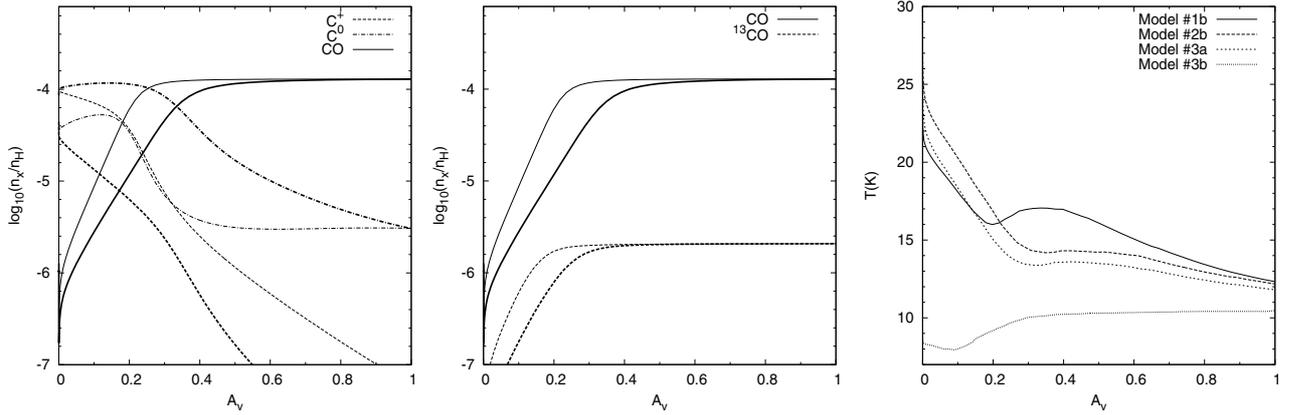
Fig. 4. *Left panel*: The abundance profile of C^+, C^0, and CO for Model #1b (thin lines) and Model #2b (thick lines) are compared. *Central panel*: The abundance profile of CO and ^{13}CO for Model #1b (thin lines) and Model #2b (thick lines). *Right panel*: Gas temperature at the cloud surface as a function of A_v for models #1b, #2b, #3a, and #3b.
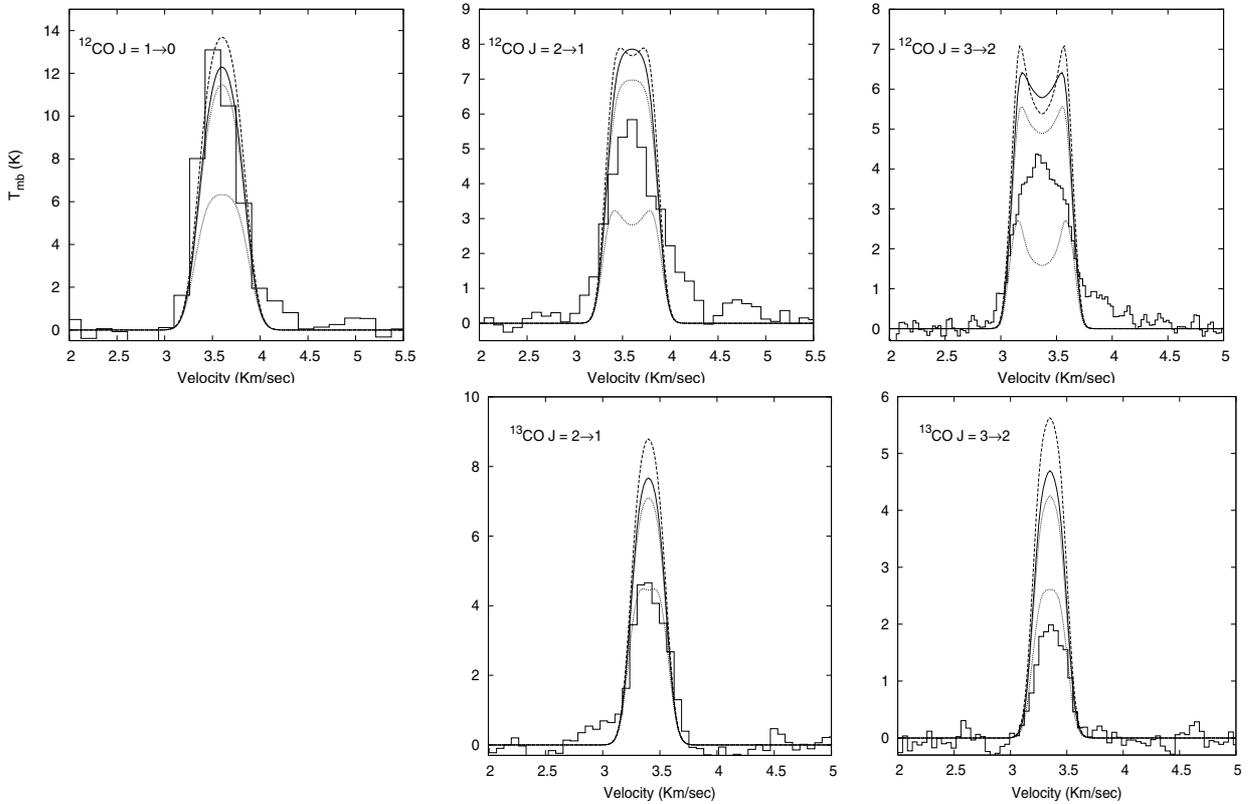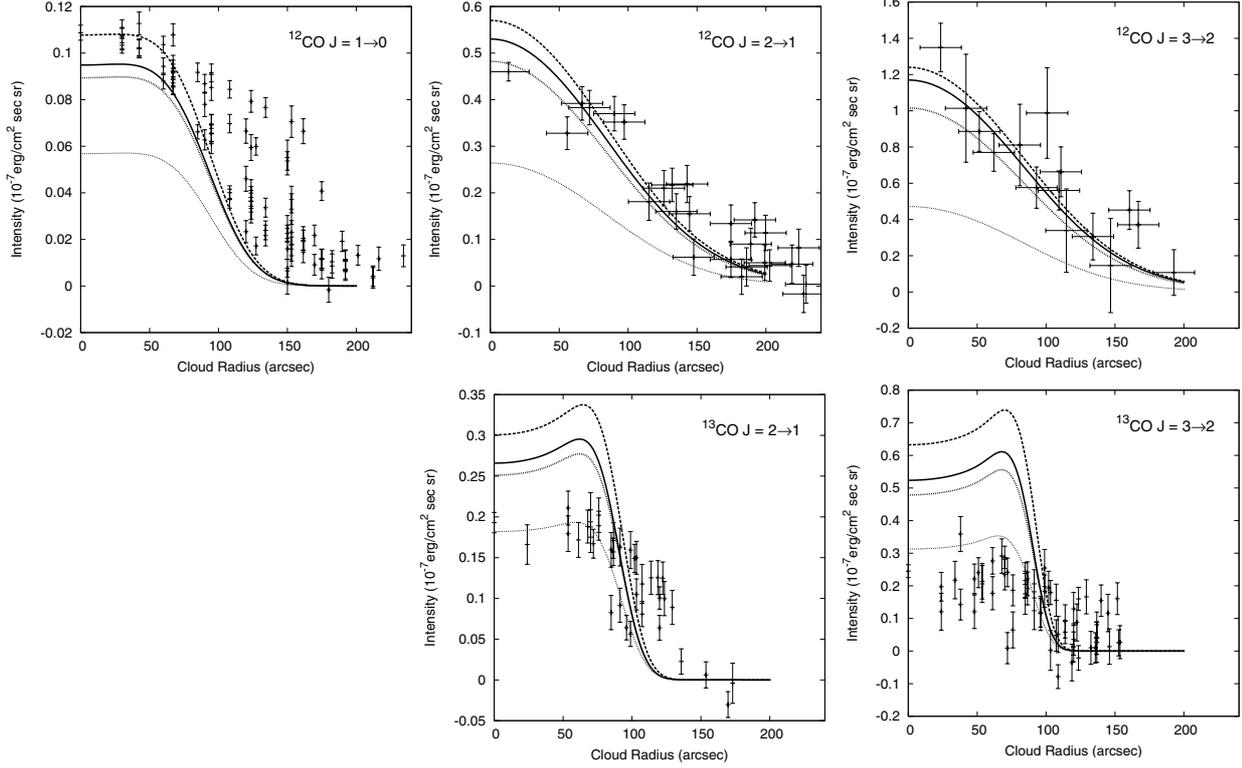

Fig. 5. Observed line profiles compared with Model #1b (dashed), #2b (solid), #3a (thick dotted), and #3b (thin dotted). The transitions are indicated in the upper left corner of each panel.

While the line intensities of both species, [C I] and CO, are reduced for a lower χ, the [C I] emission is more sensitive to the intensity of the external FUV field than the CO rotational transitions. A weaker FUV radiation field significantly decreases the gas temperature at the cloud surface (Fig. 4a) but does not change the C^0 density appreciably (Fig. 4b). Generally, the gas temperature in the models is below 23.6 K, the excitation energy of the carbon $^3P_1$ level above the ground state. In this domain the [C I] line intensity is very sensitive to the temperature and thus to χ. In contrast, reducing the FUV intensity only results in small changes of the gas temperature in the region where CO is the most abundant carbon species and thus has a correspondingly low impact on the optically thick CO lines. The exception is Model # 3b with an extremely low FUV radiation field

of $\chi = 0.12\chi_0$. In this case the cosmic-ray heating already prevails at $A_v \gtrsim 0.4$, with even *lower* temperatures closer to the surface (Fig. 4).

The strength of the FUV radiation field also influences the self-absorption in the model ^{12}CO $J = 2 \rightarrow 1$ and $J = 3 \rightarrow 2$ line profiles, because the degree of self-absorption depends on the gas temperature at the cloud surface. As these transitions are sub-thermally excited at the lower-density gas near the cloud edge, the reduction of the gas temperature in the low-FUV model results in stronger self-absorption (Fig. 5).

The lower FUV intensity significantly reduces the [C I] and ^{13}CO emission. The model with $\chi = 0.12\chi_0$ (Model #3b) reproduces the observed ^{13}CO intensities and line-integrated intensity profiles to within ~40%, confirming the results by

Fig. 6. Line-integrated intensities as a function of cloud radius. The transitions are indicated in the upper right corner of each panel. The observations (error bars) are compared with predictions for Model #1b (dashed), #2b (solid), #3a (thick dotted), and #3b (thin dotted). Horizontal error bars in the ^{12}CO $J = 2 \rightarrow 1$ and $J = 3 \rightarrow 2$ emission correspond to the uncertainly in the correction for the receiver beam offset for the KOSMA observations (see Sect. 2). We excluded the lower half of the Barnard 68 data from comparison to the CO data because of the significant deviation from the spherical symmetry, visible in the dust extinction maps (Alves et al. 2001).

Table 6. Model comparison with observed cloud intensity profiles.

| Species transition	$N^{-1}\Sigma_i^N I_{model}/I_{obs}^a$			
	Model #1b	Model #2b	Model #3a	Model #3b
^{12}CO $J = 1 \rightarrow 0$	0.95	0.82	0.78	0.50
^{12}CO $J = 2 \rightarrow 1$	1.10	0.98	0.90	0.48
^{12}CO $J = 3 \rightarrow 2$	1.10	1.00	0.87	0.40
^{13}CO $J = 2 \rightarrow 1$	1.78	1.49	1.40	0.98
^{13}CO $J = 3 \rightarrow 2$	3.28	2.60	2.39	1.50

^{a} Sum over all positions with $r < 100''$.

Table 7. Predicted line-integrated intensities toward Barnard 68 center.

Species transition	Resolution - Instrument	Intensity (10^{-7} erg s^{-1} cm^{-2} sr^{-1})			
		Model #1a	Model #1b	Model #2b	Model #3a
[C II] $^2P_{3/2} \rightarrow {}^2 P_{1/2}$	18''-GREAT-SOFIA	9.49	9.49	4.77	2.44
	13''-HIFI-Herschel	9.47	9.47	4.76	2.43
[C I] $^3P_2 \rightarrow {}^3 P_1$	25''-NANTEN2	2.83	2.86	6.65	5.43
	25''-HIFI-Herschel				
	8''-APEX	2.83	2.86	6.62	5.40
^{12}CO $J = 5 \rightarrow 4$	39''-HIFI-Herschel	2.49	2.38	1.60	1.37
	56''-CASIMIR-SOFIA	2.51	2.39	1.61	1.37
^{12}CO $J = 4 \rightarrow 3$	13''-APEX	2.22	2.12	1.83	1.56
	45''-NANTEN2	2.23	2.13	1.84	1.56

Bergin et al. (2006). However, this model cannot account for the observed [C I] and ^{12}CO emission, which is underestimated by a factor of $\gtrsim 2$. Additionally, we note that models with a low FUV radiation field produce clear self-absorption in the ^{12}CO $J = 2 \rightarrow 1$ and $J = 3 \rightarrow 2$ line profiles, which has not been observed. The model with a slightly reduced FUV radiation field ($\chi = 0.75\chi_0$; Model #3a) reduces the [C I] and ^{13}CO emission by 10% compared to the $\chi = 1.0\chi_0$ model. While the ^{12}CO model intensity still marginally agrees with the data (within $\lesssim 30\%$), the ^{13}CO emission is significantly higher than observed. Any further
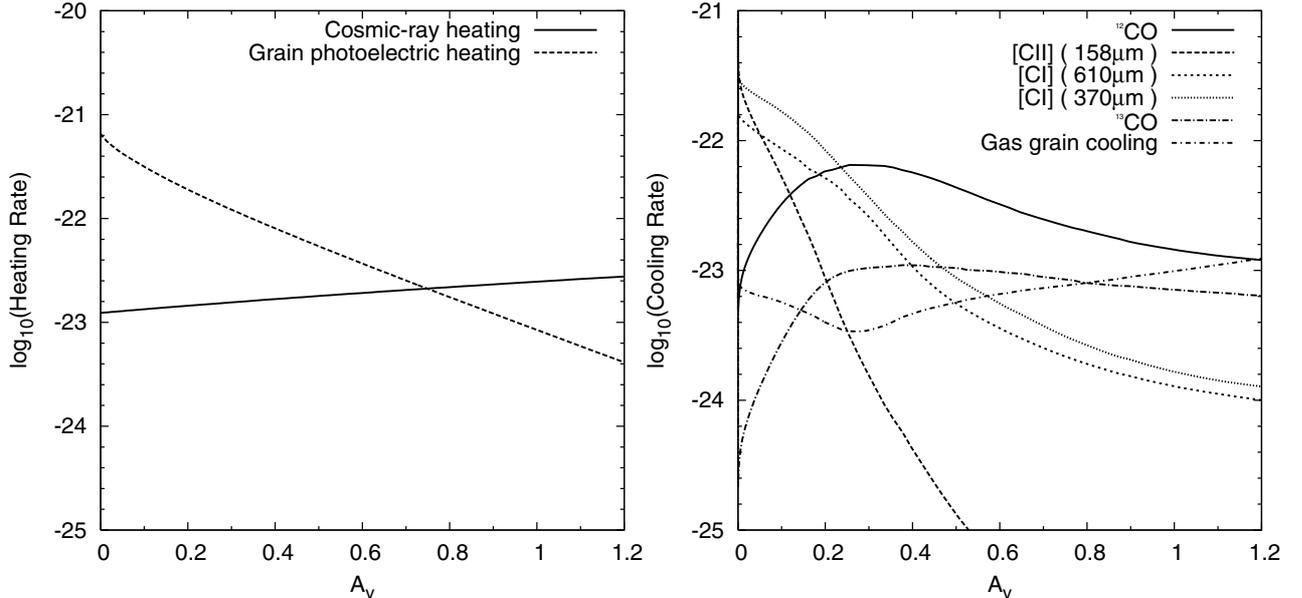
Fig. 7. Dominant heating and cooling processes for Model #3a ($\chi = 0.75\chi_0$). The heating and cooling rates are in units of erg s^{-1} cm^{-3}.

reduction brings the ^{13}CO model intensity closer to the observations, but at the same time gives [C I] and ^{12}CO intensities that are too low.

We notice that the model predictions for the ^{12}CO $J = 1 \rightarrow 0$ integrated intensity profile show larger discrepancies at radii between 90″ and 150″. This is possibly due to deviations from spherical symmetry at angular scales $\lesssim 60″$ (note, for example, the deviations in the iso-intensity contours from circular symmetry in Fig. 2; recall that we excluded the southern half of Barnard 68 for the same reason, see Fig. 6). These deviations are therefore more noticeable in the high-angular resolution ^{12}CO $J = 1 \rightarrow 0$ map than in the KOSMA maps (angular resolution 130″). We checked for any possible contribution from stray emission from the Mopra error beam (~60″, Ladd et al. 2005) and concluded that this cannot account for a significant fraction of the excess emission observed at 90″ $\lesssim r \lesssim$ 150″. Also note that emission from a low-A_v region at 100 $\lesssim r \lesssim$ 120 (Fig. 3) cannot account for this excess (see discussion in Sect. 4.1).

5. Discussion

5.1. Influence of the radiation field

We find that it is not possible to find a PDR model that matches all observations for the given density profile of Barnard 68. The main difficulty is to simultaneously match the ^{12}CO and ^{13}CO transitions. The weak ^{13}CO lines suggest a low FUV intensity of $\chi = 0.12\chi_0$, but underestimate the [C I] and ^{12}CO intensity by up to a factor of ~2 and produce deep self-absorbed ^{12}CO line profiles towards the cloud center. The ^{12}CO and [C I] intensities suggest a moderately reduced FUV field $\chi = 1-0.75\chi_0$. However, this overestimates the ^{13}CO intensity by a factor of 1.5–2.5. A strength of the FUV field on the order of the mean interstellar radiation field have been independently inferred from observations at 7 μm and 90 μm by Galli et al. (2002) (~2.5 G$_0$, corresponding to ~ 1.5χ_0), arguing against a substantial reduction of the FUV field at the location of Barnard 68. A lower impact is noticed by including PAHs in the chemical network of the model. The [C I] intensity is increased by 60%, while the CO intensity is reduced by 20%. PAHs help to remove or

reduce the self-absorption and make the line profiles more consistent with the observations. Finally, we note that depletion affects the observed transitions only to a small degree.

Observations of higher-J CO, [C I] ^{3}P$_2 \rightarrow ^3$P$_1$, and [C II] transitions are useful for distinguishing between the impact of relevant model parameters and whether the low ^{13}CO intensities indeed result from a low FUV field. They will also allow us to better assess the impact of PAHs and/or depletion due to freezing on dust even at the cloud surface. Predictions for Model #1b, #2b, #3a, and #3b are listed in Table 7 for observations with present and future observatories. The impact of PAHs is a reduction of the [C II] intensity by a factor of 2, while the [C I] ^{3}P$_2 \rightarrow ^3$P$_1$ intensity is increased by the same factor. Because of their high excitation energy, both the [C II] and [C I] ^{3}P$_2 \rightarrow ^3$P$_1$ transitions are *very* sensitive to the FUV field. They are reduced by up to a factor of 0.5 when the FUV field is reduced to $\chi = 0.75\chi_0$ and by as much as a factor of 1.4×10^{-4} for $\chi = 0.12\chi_0$. The ^{12}CO $J = 5 \rightarrow 4$ and $J = 4 \rightarrow 3$ line intensities are more moderately reduced. Together, the inclusion of PAHs and a somewhat lower FUV field ($\chi = 0.75\chi_0$) reduce them by 40%.

The detection of the ^{12}CO $J = 4 \rightarrow 3$ (APEX, NANTEN2) and ^{12}CO $J = 5 \rightarrow 4$ (HIFI Herschel, GREAT SOFIA) transitions can be obtained within a few minutes or less of observing time. A substantially longer integration time is required for the [C II] ^{2}P$_{3/2} \rightarrow ^2$ P$_{1/2}$ transitions. The detection of the [C I] ^{3}P$_2 \rightarrow ^3$P$_1$ transition might also prove very difficult from ground-based observatories. However, with HIFI-Herschel, the [C I] ^{3}P$_2 \rightarrow ^3$P$_1$ transition can be detected in less than a minute.

5.2. Heating and cooling

In Fig. 7 we show the heating and cooling for different processes as a function of the visual extinction A_v (Model #3a, $\chi = 0.75\chi_0$). Photoelectric heating dominates the gas heating at $A_v \lesssim 0.8$, being replaced by cosmic-ray heating at larger depths. The gas cooling is governed by the [C I] ^{3}P$_1 \rightarrow ^3$ P$_0$ and ^{3}P$_2 \rightarrow ^3$ P$_1$ fine-structure transitions for $A_v < 0.2$, and by the ^{12}CO (and ^{13}CO) rotational transitions for $0.2 < A_v < 1.2$. Gas-grain coupling dominates at $A_v > 1.2$. It is interesting to note that the [C II]

Table 8. Line-integrated intensity averaged over the projected clump area for Model #3a ($\chi = 0.75\chi_0$).

Species transition	Intensity (10^{-7} erg s^{-1} cm^{-2} sr^{-1})
[C II] $^2P_{3/2} \rightarrow ^2P_{1/2}$	3.94
[C I] $^3P_1 \rightarrow ^3P_0$	3.76
[C I] $^3P_2 \rightarrow ^3P_1$	6.95
^{12}CO $J = 3 \rightarrow 2$	1.19
^{12}CO $J = 4 \rightarrow 3$	1.38
^{12}CO $J = 5 \rightarrow 4$	1.13
^{13}CO $J = 2 \rightarrow 1$	0.23
^{13}CO $J = 3 \rightarrow 2$	0.45
^{13}CO $J = 4 \rightarrow 3$	0.30

transition does not dominate the cooling in this case, even very close to the cloud surface (C$^+$ dominates only at $A_v \lesssim 0.05$).

Table 8 lists the line emission averaged over the projected cross section of the clump for Model #3a ($\chi = 0.75\chi_0$). The [C I] fine-structure transitions dominate with a total intensity of 1.1×10^{-6} erg s^{-1} cm^{-2} sr^{-1}, followed by the ^{12}CO and ^{13}CO rotational transitions with a total intensity of 4.7×10^{-7} erg s^{-1} cm^{-2} sr^{-1}. The [C II] $^2P_{3/2} \rightarrow ^2 P_{1/2}$ fine-structure transition contributes with a total intensity of 3.9×10^{-7} erg s^{-1} cm^{-2} sr^{-1}. This relatively low value is attributed to the low FUV radiation field of Model #3a and to the presence of PAHs in the chemical network of the model, which significantly decreases the abundance of C$^+$ close to the surface of the cloud.

6. Summary and conclusions

We present simulations with a spherical PDR code to model the line emission in Barnard 68. Its approximately spherical geometry makes Barnard 68 an ideal test for such a spherically-symmetric PDR model. We compared the model results with the line profiles and the azimuthally averaged intensity profiles of the three lowest rotational transitions of ^{12}CO, ^{13}CO $J = 3 \rightarrow 2$, $J = 2 \rightarrow 1$, and the spatially and spectrally unresolved [C I] $^3P_1 \rightarrow ^3 P_0$ transition. This is the first time that a spherical PDR code was used to model the line emission in a low-FUV cloud in such detail.

We have tested the impact of PAHs in the chemical network of the model, of small variations on the FUV radiation field intensity, and considered the effects of depletion. The impact on the emerging ^{12}CO, ^{13}CO, [C I], and [C II] line emission is quantified. We find evidence that PAHs play a role in the chemical network. This results on a larger C^0 layer, while the C$^+$ layer is very thin, making the [C II] emission very faint and difficult to distinguish from emission from the ambient warm ionized medium in spectrally unresolved observations. Depletion is not likely to play an important role in the observed transitions.

We find it difficult to simultaneously model the observed ^{12}CO and ^{13}CO emission, with residual differences up to a factor of 2 between PDR models and observed line intensities. The weak ^{13}CO line intensity seems to require a steep drop in either the excitation conditions or in the abundances in a layer between the regions that dominate the ^{12}CO and ^{13}CO emission, respectively. A model with a low external FUV field (see also Bergin et al. 2006) is clearly incompatible with the ^{12}CO and [C I] observations. In order to reduce the ^{13}CO line emission, a shift of the ^{13}CO abundance to a region where cosmic rays dominate the

gas heating ($A_v > 0.8$) is required. However, isotope-selective reactions produce the opposite effect and a ^{13}CO abundance corresponding to the ^{13}C isotope abundance is reached in a region that is even closer to the cloud surface than for ^{12}CO (Fig. 4). Consequently, the low$-J$ ^{13}CO emission is optically thick at $A_v = 0.3-0.5$ where the gas heating is still dominated by the external FUV radiation field (Fig. 7). Including PAHs in the model reduces the gas temperature in the region where ^{13}CO is emitted, but this effect turns out to be insufficient. The ^{13}CO intensity could be significantly reduced if the gas-grain collisions dominate the cooling closer to the surface and the dust temperature is close to ~10 K. However, a confirmation of the low observed ^{13}CO intensity is also highly desirable. Together with observations of mid$-J$ ^{12}CO, [C I], and [C II] transitions with present and future telescopes (NANTEN2, APEX, SOFIA, Herschel), this will allow us to test our results and assess the importance of different model parameters.

References

Alves, J. F., Lada, C. J., & Lada, E. A. 2001, Nature, 409, 159
Bakes, E. L. O., & Tielens, A. G. G. M. 1994, ApJ, 427, 822
Bakes, E. L. O., & Tielens, A. G. G. M. 1998, ApJ, 499, 258
Bergin, E. A., Maret, S., van der Tak, F. F. S., et al. 2006, ApJ, 645, 369
Bergin, E. A., & Snell, R. L. 2002, ApJ, 581, L105
Bourke, T. L., Hyland, A. R., Robinson, G., James, S. D., & Wright, C. M. 1995, MNRAS, 276, 1067
de Geus, E. J., de Zeeuw, P. T., & Lub, J. 1989, A&A, 216, 44
Di Francesco, J., Hogerheijde, M. R., Welch, W. J., & Bergin, E. A. 2002, AJ, 124, 2749
Draine, B. T. 1978, ApJS, 36, 595
Draine, B. T., & Sutin, B. 1987, ApJ, 320, 803
Galli, D., Walmsley, M., & Gonçalves, J. 2002, A&A, 394, 275
Gierens, K. M., Stutzki, J., & Winnewisser, G. 1992, A&A, 259, 271
Habing, H. J. 1968, Bull. Astron. Inst. Netherlands, 19, 421
Hollenbach, D. J., & Tielens, A. G. G. M. 1997, ARA&A, 35, 179
Hollenbach, D. J., & Tielens, A. G. G. M. 1999, Rev. Mod. Phys., 71, 173
Hotzel, S., Harju, J., & Juvela, M. 2002a, A&A, 395, L5
Hotzel, S., Harju, J., Juvela, M., Mattila, K., & Haikala, L. K. 2002b, A&A, 391, 275
Kaufman, M. J., Wolfire, M. G., Hollenbach, D. J., & Luhman, M. L. 1999, ApJ, 527, 795
Ladd, N., Purcell, C., Wong, T., & Robertson, S. 2005, Pub. Astron. Soc. Aust., 22, 62
Le Bourlot, J., Pineau Des Forets, G., Roueff, E., & Flower, D. R. 1993, A&A, 267, 233
Lepp, S., & Dalgarno, A. 1988, ApJ, 324, 553
Mathis, J. S., Rumpl, W., & Nordsieck, K. H. 1977, ApJ, 217, 425
Melnick, G. J., Stauffer, J. R., Ashby, M. L. N., et al. 2000, ApJ, 539, L77
Röllig, M., Abel, N. P., Bell, T., et al. 2007, ArXiv Astrophysics e-prints
Störzer, H., Stutzki, J., & Sternberg, A. 1996, A&A, 310, 592
Tielens, A. G. G. M., & Hollenbach, D. 1985, ApJ, 291, 722
van Dishoeck, E. F., & Black, J. H. 1988, ApJ, 334, 771